

Journal of Materials Chemistry C

Accepted Manuscript



This is an *Accepted Manuscript*, which has been through the Royal Society of Chemistry peer review process and has been accepted for publication.

Accepted Manuscripts are published online shortly after acceptance, before technical editing, formatting and proof reading. Using this free service, authors can make their results available to the community, in citable form, before we publish the edited article. We will replace this *Accepted Manuscript* with the edited and formatted *Advance Article* as soon as it is available.

You can find more information about *Accepted Manuscripts* in the [Information for Authors](#).

Please note that technical editing may introduce minor changes to the text and/or graphics, which may alter content. The journal's standard [Terms & Conditions](#) and the [Ethical guidelines](#) still apply. In no event shall the Royal Society of Chemistry be held responsible for any errors or omissions in this *Accepted Manuscript* or any consequences arising from the use of any information it contains.

ARTICLE

The Gold-rich $R_3Au_7Sn_3$: Establishing the Interdependence between Electronic Features and Physical Properties

Cite this: DOI: 10.1039/x0xx00000x

Received 00th January 2015,
Accepted 00th January 2015

DOI: 10.1039/x0xx00000x

www.rsc.org/

Alessia Provino,^{a,b} Simon Steinberg,^{a,c} Volodymyr Smetana,^{a,c} Ruta Kulkarni,^d
Sudesh K. Dhar,^d Pietro Manfrinetti,^{*a,b,e} Anja-Verena Mudring^{*,a,c}

Two new polar intermetallic compounds $Y_3Au_7Sn_3$ (**I**) and $Gd_3Au_7Sn_3$ (**II**) have been synthesized and their structures have been determined by single crystal X-ray diffraction ($P6_3/m$; $Z = 2$, $a = 8.148(1)/8.185(3)$, $c = 9.394(2)/9.415(3)$ for **I/II**, respectively). They can formally be assigned to the $Cu_{10}Sn_3$ type and consist of parallel slabs of Sn centered, edge-sharing trigonal Au_6 antiprisms connected through R_3 ($R = Y, Gd$) triangles. Additional Au atoms reside in the centres of trigonal Au_6 prisms forming $Au@Au_6$ clusters with Au–Au distances of 2.906–2.960 Å, while the R – R contacts in the R_3 groups are considerably larger than the sums of their metallic radii. These exclusive structural arrangements provide alluring systems to study the synergism between strongly correlated systems, particularly, those in the structure of (**II**), and extensive polar intermetallic contacts, which has been inspected by measurements of the magnetic properties, heat capacities and electrical conductivities for both compounds. $Gd_3Au_7Sn_3$ shows an antiferromagnetic ordering at 13 K, while $Y_3Au_7Sn_3$ is a Pauli paramagnet and a downward curvature in its electrical resistivity at about 1.9 K points to a superconducting transition. DFT-based band structure calculations on $R_3Au_7Sn_3$ ($R = Y, Gd$) account for the results of the conductivity measurements and different spin ordering models of (**II**) provide conclusive hints into its magnetic structure. Chemical bonding analyses for both compounds indicate that the vast majority of bonding originates from the heteroatomic Au–Gd and Au–Sn interactions, while homoatomic Au–Au bonding is evident for the $Au@Au_6$ clusters.

Introduction

Polar intermetallic compounds of electropositive metals (group 1-3; A, Ae, R), late transition (group 11) and post transition (group 13-15; X) elements have attained an increased interest due to their complex structural formations, valuable physical properties and unusual bonding characteristics.¹ Although the systems A/Ae -Au- X have been intensively examined,¹ yet, the related systems with rare earth metals (R) have been studied to a lesser extent and are known mainly for a series of isostructural compounds, in particular, the stoichiometric $RAuX^{2-4}$ and R_2Au_2X phases.^{5,6} The properties of these compounds are quite diverse and include Kondo effects, thermoelectricity, superconductivity or hydrogen storage ability suitable for emerging applications.⁷ After the recent discoveries of localized magnetic moments in $i-RCd_{7,7}$ phases ($R = Gd$ to Tm)⁸ some R -Au- X systems ($R = Ce, Eu, Gd, Tm$), which are known to form several quasicrystal (QC) approximants,⁹ have become prospective fields of interest to study the nature of magnetic interactions in aperiodic lattices.

Among the R -Au- X systems the Au-rich materials attracted our interest to scrutinize the impact of the relativistic effects of gold^{10,11} on their formations, bonding and properties due to the enhanced participation of Au in hetero- or homoatomic clusters and networks, which are typically formed in simple binary solid solutions and

complex metallic alloys including QCs and their approximants.¹²⁻²¹ Recent investigations of the R -Au-Sn systems identified several compounds with characteristic equiatomic R and X contents as well as compositions, which deviate from the ideal values because of mixed site or partial site occupancy. Four phases with the stoichiometric compositions $Yb_2Au_3Sn_2$,²² $R_3Au_4Sn_3$ ($R = La-Nd$), $R_5Au_8Sn_5$ ($R = Sm, Gd$) and $La_4Au_7Sn_4$ are observed for a narrow range from 27 to 30 at.% R^{23} and belong to a family with the general formula $R_{m+n}T_{2m+n}Sn_{m+n}$ ($T = Ni, Cu, Au$), which are built up by m slabs of the $GdPt_2Sn$ type²⁴ and n slabs of the $SrPtSb$ type.²⁵ The first one is formed by edge-sharing Pt trigonal antiprisms sandwiched between two rare earth layers, while the second slab corresponds in fact with the whole cell of a ternary ordered AlB_2 type.

The next representative of the family and first compounds with more than 50 at.% of Au – $R_3Au_7Sn_3$ was detected with Y and Gd during systematic investigations of the corresponding ternary systems and is composed of layers of trigonal centered Au_6Sn antiprisms as well as homoatomic $Au@Au_6$ clusters that are surrounded by R triangles. This exclusive structural arrangement allows revealing the cooperative impact of strongly correlated electrons, which control the particular properties of the lanthanides,²⁶ and extensive polyanionic host lattices on the properties of the materials. Therefore, we investigated the structure, magnetic, electric and

thermal properties and electronic structures in the novel Au-rich $R_3\text{Au}_7\text{Sn}_3$ ($R = \text{Y}, \text{Gd}$).

Results and discussion

Crystal chemistry.

Since all structural parameters are nearly identical for both phases, the structure of the Gd-containing compound (**II**) will be discussed as a representative of both compounds. The crystal structures of $\text{Y}_3\text{Au}_7\text{Sn}_3$ (**I**) and $\text{Gd}_3\text{Au}_7\text{Sn}_3$ (**II**) are best described in terms of two kinds of alternating slabs; however, the scheme applied for previously reported $R_{m+n}T_{2m+n}\text{Sn}_{m+n}$ compounds²³ fails here.

The structures are characterized by Sn-centered Au_6 trigonal antiprisms, a structural feature common of all $R_{m+n}T_{2m+n}\text{Sn}_{m+n}$ compounds. However, in this case no R atoms centre the trigonal prisms, and, in consequence, SrPtSb-type slabs cannot be observed. Edge-sharing Au_6Sn antiprisms, formed by Au2 atoms (Wyckoff site 12i) and centred by Sn4 (Wyckoff site 4f) and Sn5 (Wyckoff site 2b) give rise to slabs (**A**, Figure 1) in the ab plane. Owing to the two inequivalent tin positions, these units differ not only in their somewhat different Au–Sn contacts (the Sn5-centered unit is more regular), but also with respect to their second coordination environment. In particular, (see **B**, Figure 1), the Au_6Sn clusters located on the c axis are surrounded by additional trigonal Gd_6 antiprisms, while Au_6Sn clusters inside the unit cell are axially capped by one Au1 atom and a Gd_3 triangle. Au–Sn distances within the **A** slabs are also quite long with 2.845(1)–2.952(1) Å.

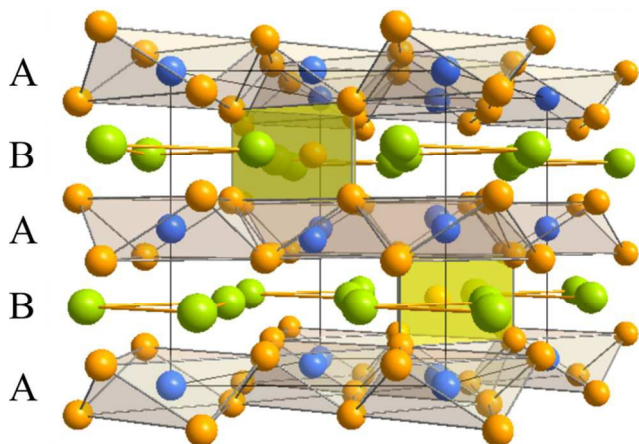


Figure 1 The crystal structure of $R_3\text{Au}_7\text{Sn}_3$, central projection. Au atoms are marked orange, tin – blue and Y(Gd) – green.

The Au1 position (Wyckoff site 2d) is quite unusual. Surrounded by six Au2 atoms, it centres the unique trigonal prismatic $\text{Au}@_6$ formation. To the best of our knowledge, such an Au_7 fragment has not been observed in the solid state. The trigonal Au_6 prism is considerably squashed with $d_{\text{Au–Au}} = 2.906(2)$ Å along the c axis and 4.467(2) Å in the ab plane. Au–Au interatomic contacts from the centre to the prism vertices are 2.960(1) Å. Thus, it is probably more appropriate to describe the $\text{Au}@_6$ unit as being composed of three vertex-sharing isosceles (almost equilateral) Au_3 triangles forming a propeller. Each Au_6 prism is in turn capped axially by two Sn4 atoms and equatorially by three Gd atoms (Figure 2). It is worth noting that the Au1–Sn4 and Au1–Gd contacts are quite short – 2.753(2) Å and 2.956(2) Å, respectively, values which, in fact, represents well the actual sums of the corresponding covalent radii.²⁷ Still, the for-

mer are significantly shorter than the Au–Sn separations (2.845(1)–2.952(1) Å) in the Au_6Sn antiprisms of the **A** slabs. It is worth noting that the latter are also significantly squashed in accordance with the $\text{Au}@_6$ fragment. The presence of large R atoms in the **B** layers is an important factor for the shape of the $\text{Au}@_6$ units.

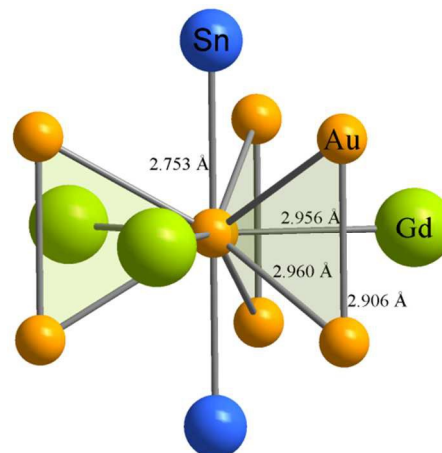


Figure 2 Coordination polyhedron of Au1 in the crystal structure of $\text{Gd}_3\text{Au}_7\text{Sn}_3$.

The Au–Au distances within the $\text{Au}@_6$ groups, 2.906–2.960 Å, are slightly longer than commonly observed for compounds in the $A\text{–Au–}X$ systems;[†] however, they are definitely shorter than those observed within the Au_6Sn layers – 3.147(2) Å and 3.339(2) Å, respectively. For comparison, Au–Au distances observed for the hexagonal diamond-like Au lattices in the rhombohedral $\text{Ba}_2\text{Au}_{8.06}\text{Sn}_{0.94}$ ²⁸ range from 2.877 to 3.393 Å within the chair-like Au_6 hexagons and are equidistant between the Au layers – 3.094 Å. $\text{Ba}_2\text{Au}_{8.06}\text{Sn}_{0.94}$ and a series of related compounds $Ae(\text{Au}, X)_7$ and $Ae_2(\text{Au}, X)_9$ ^{29–33} were described on the basis of the hexagonal diamond Au-networks with encapsulated cations and anionic groups. Alternatively, the structure of $\text{Gd}_3\text{Au}_7\text{Sn}_3$ can be described as Gd_3 capped Au_7 units sandwiched between two Sn_6 hexagons in chair conformation (Figure 3). The latter share faces with six identical polyhedra within the same slab and show partial overlap with three polyhedra above and below along the c axis. Thus, in spite of non-bonding contacts, the Sn substructure can be described in terms of a classical diamond network.

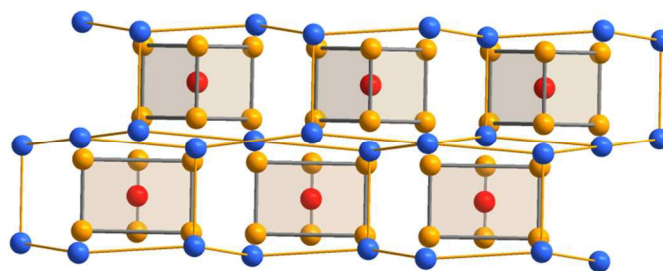


Figure 3 $\text{Au}@_6$ clusters sandwiched between the hexagonal layers of $\text{Sn}@_6$ in the crystal structure of $\text{Gd}_3\text{Au}_7\text{Sn}_3$ (orthorhombic projection). The endohedral Au position is marked red, Au_6 prisms – orange and Sn layers – blue, respectively; Y(Gd) atoms are omitted for clarity.

The closest structural analogue to the Au₇ cluster can be derived from the crystal structure of Rb₄Au₇Sn₂.³⁴ This compound crystallizes with the rhombohedral space group *R*-3*m* (no. 166) and exhibits structural motifs similar to those in the present *R*₃Au₇Sn₃ structures. One of such motifs is an Au₇-related unit formed by two Au vertex-sharing tetrahedra. In another way, this polyhedron can be described as an Au centered trigonal Au₆ prism; however, in contrast what is observed in hexagonal *R*₃Au₇Sn₃, these prisms are strongly elongated. Thus, this may be regarded as the opposite case with comparable short Au–Au contacts on the bases and long edges along the axis. It is interesting that the Cu₉Sn₃ group in Cu₁₀Sn₃³⁵ is also slightly different with shortest Cu–Cu distances from the centre to the edges and relatively long axial Cu–Cu contacts, which correspond to the shortest Au–Sn bonds in the gadolinium compound.

*R*₃Au₇Sn₃ can formally be assigned to the Cu₁₀Sn₃ structure type³⁵ and are the first ternary representatives of the latter. Sn atoms in the structure of Cu₁₀Sn₃ are fully substituted by *R* atoms, while positions of Cu are occupied by Au and Sn, respectively. The result of these substitutions emphasizes a significant role of the geometric factors in the formation of the Cu₁₀Sn₃ structure type. Although the binary and ternary phases may exhibit certain structural similarities, there are significant differences between these phases. In particular, the absolute electronegativities of Cu and Sn are almost identical – 1.90 and 1.96, respectively,³⁶ whereas band structure calculations for the ternary *R*₃Au₇Sn₃ (see Electronic structures) will reveal that they are quite polar intermetallics in contrast to Cu₁₀Sn₃. Because of the presence of relatively large cations in **I** and **II**, the volumes of the unit cells increase by ~35% compared to Cu₁₀Sn₃, yet, nearly alike structural features are retained. Note that the valence electron concentrations (electron/atom) also changes significantly from 1.7 *e*⁻/*a* in Cu₁₀Sn₃ to 2.15 *e*⁻/*a* in *R*₃Au₇Sn₃.

Besides resemblances to *R*₂Au₃Sn₂, *R*₃Au₄Sn₃, *R*₄Au₇Sn₄ and *R*₅Au₈Sn₅, *R*₃Au₇Sn₃ are also related to the ternary *RAuSn* phases (*R* = Y, Ce, Pr, Nd, Sm, Tb, Dy, Ho).³⁷ All of them crystallize in the ZrBeSi structure type,³⁸ or similar polymorph modifications. Both YAuSn and GdAuSn were reported to crystallize in ZrBeSi and its lower symmetric modification LiGaGe.^{37,39,40} *R*₃Au₇Sn₃ can be well described as polyhedral representatives of the ZrBeSi structure type: axial Au₆Sn groups occupy the positions of Zr, while Au₇Sn₂ and Gd₃ units can be assigned to the Be and Si sites, respectively. In such representation the composition of the unit cell would be (Gd₃)₂(Au_{6/2}Sn)₂(Au_{6/2}AuSn₂)₂ ≡ (Gd₃)(Au₃Sn)(Au₄Sn₂) = Gd₃Au₇Sn₃.

Physical properties.

An inspection of the magnetic susceptibility data for Gd₃Au₇Sn₃ reveals a peak near 13 K, which can be assigned to a transition from a paramagnetic to an antiferromagnetic state (see lower inset in Figure 4). The linear behaviour of the inverse magnetic susceptibility, χ^{-1} , for nearly the entire paramagnetic range indicates the presence of a spin ground state and a Curie-Weiss fit over a temperature range from 100 to 300 K yields an effective paramagnetic moment, μ_{eff} , of 8.13 μ_{B} /Gd and a Curie temperature, θ_{p} , of –8.6 K. The negative sign of θ_{p} is in full conformity with the antiferromagnetic transition near 13 K, while the magnitude of μ_{eff} is close to the Hund's rule derived value of a trivalent Gd ion (7.94 μ_{B}).²⁶ The slight excess value of μ_{eff} is tentatively attributed to conduction electron polarization. Based on the mean field theory for a spin frustrated system, in which the ordering temperature T_{N} is significantly smaller than θ_{p} ,⁴¹ geometrical frustration, akin to a canted antiferromagnet, can be excluded for the Gd network. The isothermal magnetization of Gd₃Au₇Sn₃ in fields of up to 50 kOe at 1.8 K (Figure 5) is consistent with the presence of an

antiferromagnetic state below 13 K. Additionally, a field-induced spin-flop transition is suggested for fields of around 20 kOe, but this prediction requires additional investigation. Fields higher than 50 kOe will be needed to reach full magnetic polarization for the Gd atoms. A comparison of the susceptibility data for Gd₃Au₇Sn₃ to those for the isostructural Y-containing compound indicates that the magnetic response in Gd₃Au₇Sn₃ arises solely from the Gd atoms. Particularly, the susceptibility of 9.8×10^{-4} emu/mol (7.6×10^{-5} emu/g atom) for Y₃Au₇Sn₃ at 300 K suggests a Pauli paramagnetic behaviour, which typically corresponds to a metallic state.

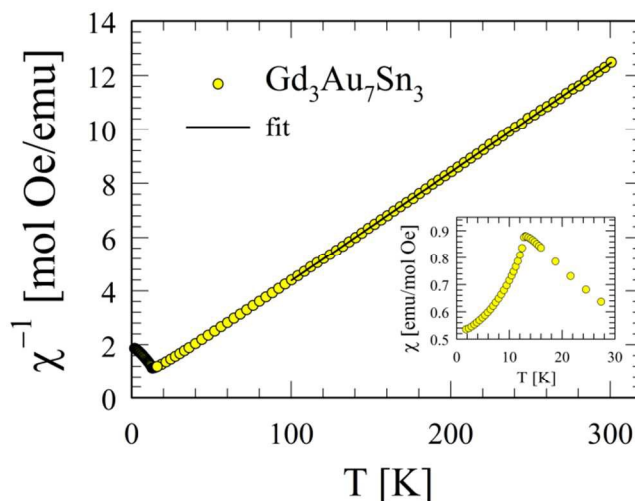


Figure 4 Inverse magnetic susceptibility, χ^{-1} , of Gd₃Au₇Sn₃; the solid line is a fit of the Curie-Weiss law to the data between 100 and 300 K. The inset shows the susceptibility, χ , below 30 K.

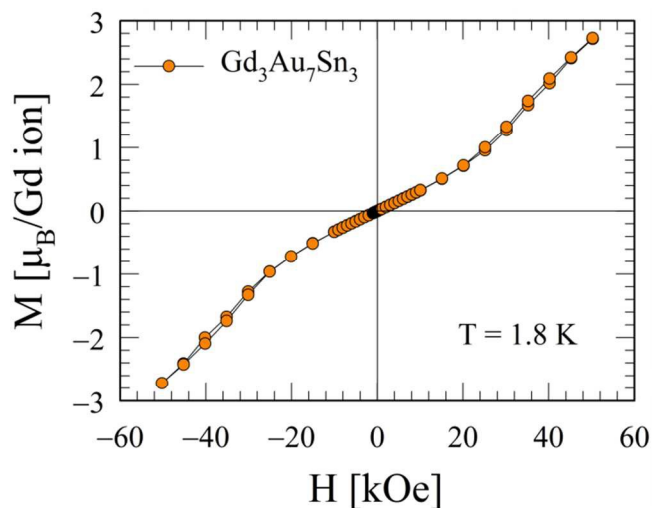


Figure 5 Isothermal magnetization loop of Gd₃Au₇Sn₃ between -50 and 50 kOe at 1.8 K.

The heat capacity of Gd₃Au₇Sn₃ is in accordance with the susceptibility data, as a huge anomaly at 12.6 K with a peak height of nearly 110 J/mol K (Figure 6) confirms the bulk magnetic ordering of the Gd atoms. For comparison, Figure 6 also depicts the heat capacity of the non-magnetic reference compound Y₃Au₇Sn₃ which

increases monotonically with temperature. From the low temperature data (below 10 K), the coefficient of the linear term of the molar heat capacity (Sommerfeld coefficient) γ is found to be 19.1 mJ/mol K² (1.5 mJ/g atom K²) in Y₃Au₇Sn₃.

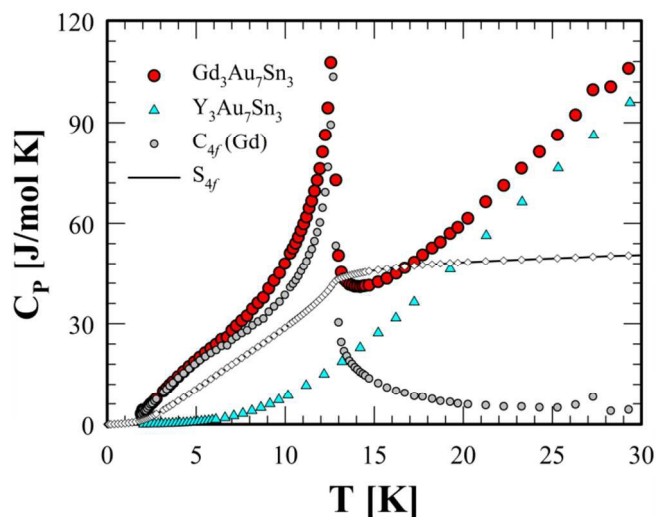


Figure 6 The molar heat capacity, C_p , of Gd₃Au₇Sn₃ and the non-magnetic reference analogue Y₃Au₇Sn₃ between 1.8 and 30 K. The magnetic contribution to the heat capacity, $C_{4f}(\text{Gd})$, and the entropy S_{4f} are also shown.

The evolution of entropy with temperature, S_{4f} , in Gd₃Au₇Sn₃ is also shown in Figure 6 and calculated by integrating C_{4f}/T with temperature. The magnetic contribution to the heat capacity, C_{4f} , was obtained based on the assumption that the phonon heat capacity of Gd₃Au₇Sn₃ is the same as that of Y₃Au₇Sn₃ after taking the different atomic masses of Y and Gd into account. The heat capacity of Y₃Au₇Sn₃ was subtracted from that of Gd₃Au₇Sn₃, after it was properly normalized due to the different atomic masses of Y and Gd, following a previously described procedure.⁴² The entropy S_{4f} reaches 50.6 J/mol K in the paramagnetic state at 30 K, which is close to the theoretical value of $3R\ln 8$ (51.8 J/mol K). Note that C_{4f} does not decrease sharply to zero above the transition, but has a residual tail, which is most likely due to the persistence of some short range order in the paramagnetic region.

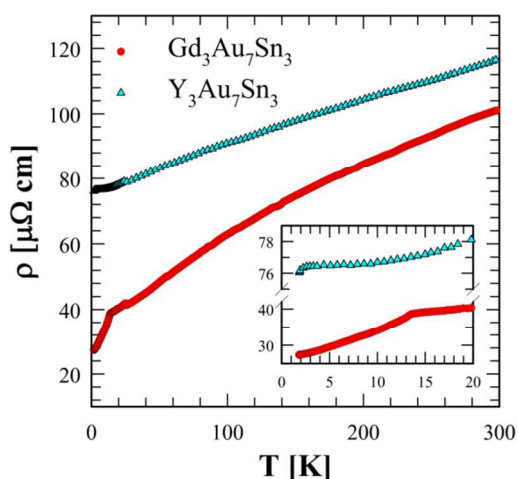


Figure 7 Electrical resistivity data of Y₃Au₇Sn₃ and Gd₃Au₇Sn₃ recorded for a range between 1.8 and 300 K. The lower inset shows the resistivity data of Y₃Au₇Sn₃ and Gd₃Au₇Sn₃ below 20 K on an expanded scale.

The electrical resistivity was measured for both Y₃Au₇Sn₃ and Gd₃Au₇Sn₃ between 1.8 and 300 K (Figure 7). Metallic behaviours are observed for both compounds as the resistivity decreases with the decline in temperature. For Gd₃Au₇Sn₃, the resistivity shows an anomaly near the magnetic transition due to the gradual freezing of the spin-disorder scattering in the magnetically ordered state. The resistivity data of both compounds below 16 K are shown in the lower inset on an expanded scale. Comparatively, no anomaly is seen down to 2 K in Y₃Au₇Sn₃, which is in conformity with its Pauli paramagnetic state. Below 2 K, the resistivity data of the yttrium-containing compound exhibit a slight downward trend, which may be a precursor to a superconducting transition. However, additional resistivity data for lower temperature ranges are needed for confirmation.

Electronic structures.

The electronic structures of $R_3\text{Au}_7\text{Sn}_3$ ($R = \text{Y, Gd}$) were analysed to provide an insight into the structure-property-relationships for these compounds. Based on the conductivity and magnetic measurements, localized 4*f* states are expected for the gadolinium-containing compound, which requires further precision.

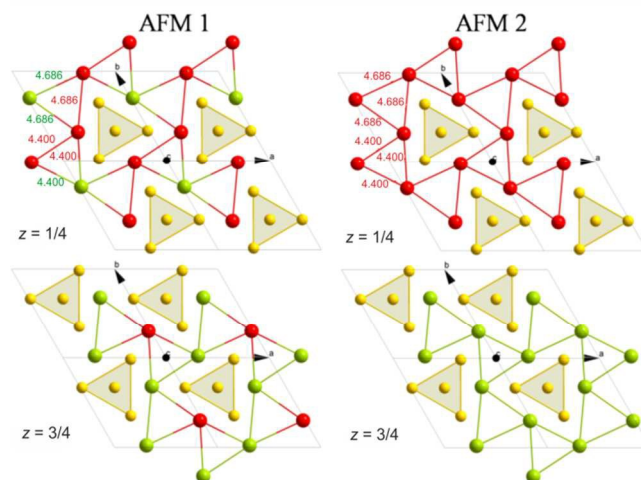


Figure 8 Representations of the antiferromagnetic orderings within the Gd lattices for the models AFM1 and AFM2: the T1 ($z = 1/4$) as well as the T2 ($z = 3/4$) layers of Gd triangles encapsulate the Au@Au₆ agglomerates, while Sn atoms have been omitted for clarity. Gd atoms with spins parallel to the c axis ("up") are coloured green, while gadolinium atoms with spins antiparallel to (001) ("down") are marked in red.

Typically, the introduction of an effective on-site Coulomb interaction term to the Kohn-Sham Hamiltonian is required for a proper treatment of the strong correlations within the highly localized gadolinium 4*f* states.⁴³ Therefore, a correctional Hubbard U parameter (see Computational details) was introduced in all VASP-based band structure calculations on the gadolinium-containing compound. To provide conclusive hints accounting for the magnetic ordering in Gd₃Au₇Sn₃, three different spin ordering models were examined: a ferromagnetic model (FM) and two independent antiferromagnetic models (AFM1 and AFM2; Figure 8 and S2–S7). In the AFM1 model the Gd triangles exhibit alternating spin orientations within the T1 and T2 layers, while the Gd groups in the AFM2 model show parallel alignments within, but antiparallel arrangements between the T1 and T2 layers (Figures S6 and S7). The Gd lattice is strongly distorted with Gd–Gd distances of 4.400 and 4.686 Å, respectively, which restrict the possibility of a direct f - f interaction akin to a canted AF model.

A comparison of the VASP-based total energies for all magnetic models reveals that there is a significant energy difference of 23 meV between the FM and the AFM2 model (Figure 9). Additionally, the latter model results in the lowest total energy and differs from the AFM1 model by about 7 meV. Accordingly, an antiferromagnetic ordering is favoured for the hexagonal $\text{Gd}_3\text{Au}_7\text{Sn}_3$, which is in full accordance with the results of the magnetic measurements. An inspection of the $E(V)$ curves for all models reveals the absence of an intersection point, which typically controls a pressure-induced transition from one state to another. Notably, the courses of all $E(V)$ curves follow third-order Birch-Murnaghan equation of states (Figure 9)⁴⁴ and the optimized structural parameters of all models show only slight deviations from the experimental parameters. For instance, the optimized lattice parameters for the lowest energy AFM2 model ($a = 8.337 \text{ \AA}$, $c = 9.590 \text{ \AA}$) are in good agreement with the experimental data (Table 1).

To analyse the outcome of the different antiferromagnetic ordering models on the electronic structure for $\text{Gd}_3\text{Au}_7\text{Sn}_3$, we followed up with an analysis of the DOS curves for both models. Additional examinations of the DOS curves for $R_3\text{Au}_7\text{Sn}_3$ ($R = \text{Y, Gd}$) provide conclusive explanations for the electric properties of both compounds.

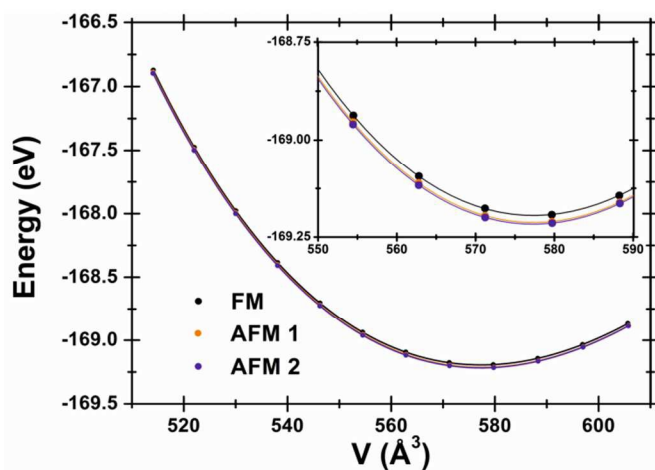


Figure 9 $E(V)$ plots for the FM, AFM1 and AFM2 spin ordering models; upper inset: magnification of the region around the minima.

Density of States.

A comparison of the spin-polarized DOS curves for the two antiferromagnetic spin ordering models of $\text{Gd}_3\text{Au}_7\text{Sn}_3$ (Figures 10 and S2) reveals an antiferromagnetic ordering state, as the spin-up and spin-down curves superimpose for both models. Furthermore, the states near the Fermi level originate from the Au d states with minor contributions from the Sn p and Gd d atomic orbitals (AOs). Notably, the Fermi levels of both models fall in minima of the DOS curves, which typically indicate an electronically favourable situation. Additionally, such characteristics in the DOS curves of both models suggest metallic conductivity for the hexagonal $\text{Gd}_3\text{Au}_7\text{Sn}_3$, which is further confirmed by conductivity measurements (see Physical properties section).

Below E_F , there are broad gaps (between -2.37 and -1.28 eV for model 1 and between -2.37 and -1.30 eV for model 2), which separate the Au d states from the Gd f states. The bands accounting for the latter are located at around -2.75 eV (model 1) and -2.76 eV (model 2), respectively, and exhibit very small dispersions suggesting rather localized states. Yet, a significant difference in the spin-

polarized DOS curves of model 1 from those of model 2 arises from the dissimilar Gd f AO contributions from the layers of isosceles Gd triangles (Figures S6 and S7). In the model 1, the contributions to the spin-up Gd f PDOS stem primarily from the T2 layers with minor contributions from the T1 layers and, vice versa, the latter exhibits major shares to the spin-down Gd f PDOS. Comparatively, spin-up Gd f states originate solely from the T2 layers in the model 2, whereas an equal sum of spin-down Gd f states derives from the T1 layers.

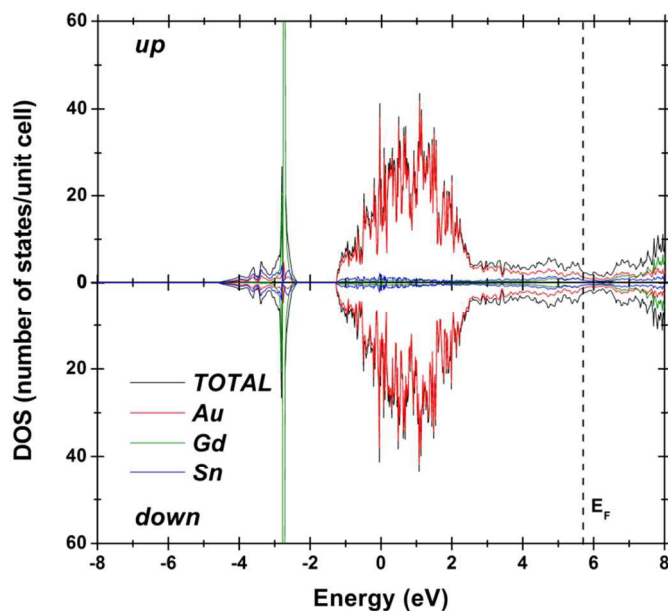


Figure 10 Plots of the spin-polarized total and projected DOS curves for the AFM spin ordering model 2. The Fermi level is represented by the dashed lines.

An inspection of the energy regions about the Fermi levels reveals that there are sharp peaks at around 8.48 eV, which may be assigned to the Gd f orbitals for both models. Such large exchange splitting of the f states by about 11.23 eV, which is observed typically for Gd-containing compounds, means that the orbital momentum nearly vanishes and also indicates that there is no direct f - f interaction.⁴³ This outcome is in accordance with Hund's rule, which predicts a well localized spin-only moment for the half-filled Gd f states. Certainly, the magnetic data of the gadolinium-containing compound point to half-filled $4f^7$ configurations for Gd as the origin of the magnetic moment. As a consequence, the electronic (and, furthermore, physical) properties of this compound are primarily controlled by the states near the Fermi level.

A major difference in the DOS curves for $\text{Y}_3\text{Au}_7\text{Sn}_3$ from those for the gadolinium-containing compound originates from the absence of the localized f -states below the Fermi level. The states near E_F arise primarily from the Au d states with minor contributions from the Y d and Sn p AOs (Figure S8). An inspection of the energy regions around these bands reveals the presence of a saddle point at E_F akin to a van Hove singularity (Figure 12),^{45,46} which may alleviate a transition to a superconducting state; however, this prediction deserves further studies of the low-temperature resistivity data for the Y-containing compound. Comparatively, such saddle point is not present at the Fermi level of the gadolinium-containing analogue, which is in fair agreement with the resistivity data of $\text{Gd}_3\text{Au}_7\text{Sn}_3$. As the Fermi level in the yttrium-containing structure falls close to a

local minimum of the DOS curves, a metallic behaviour can be inferred for $Y_3Au_7Sn_3$.

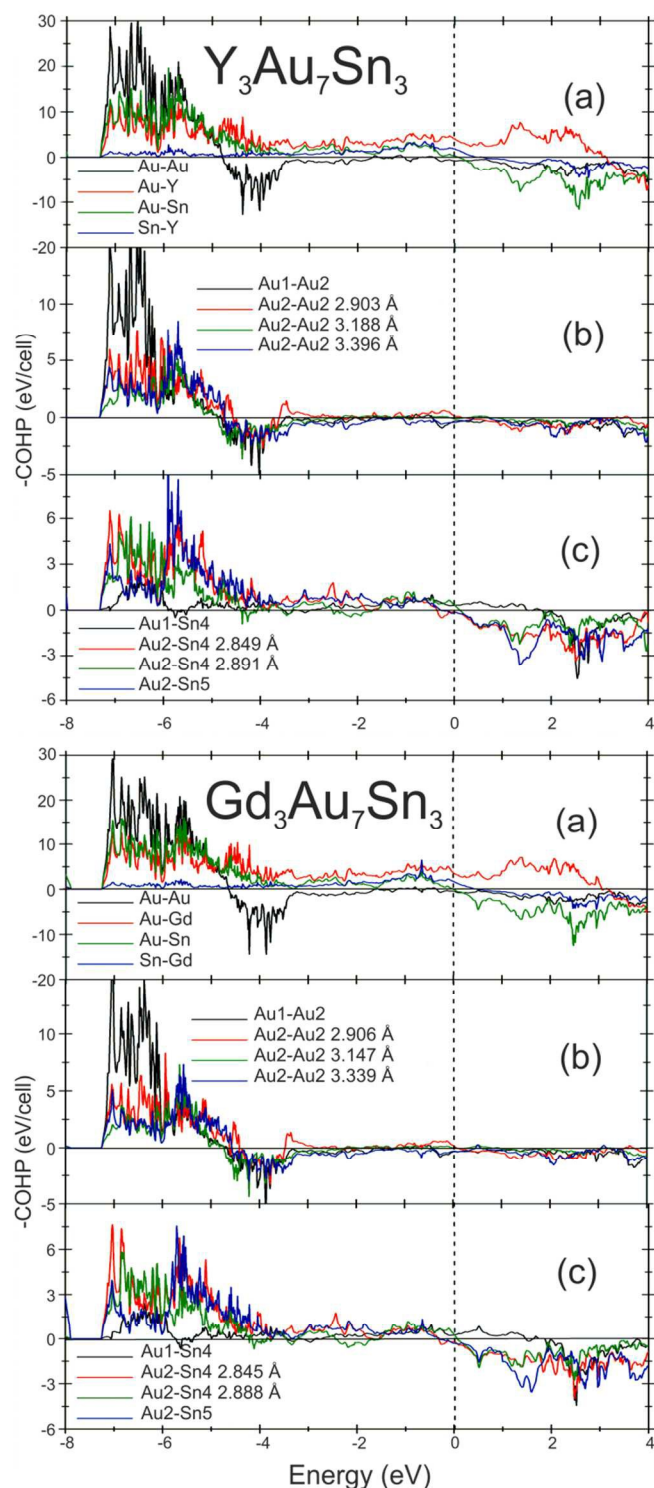


Figure 11 Total (a) and interaction-projected ((c) and (d)) -COHP curves for the hexagonal $R_3Au_7Sn_3$ ($R = Y, Gd$). Antibonding and bonding states are represented by the negative and positive contributions, respectively, while the Fermi level is represented by the dotted lines.

Bonding analysis.

A detailed picture of the bonding situation for the hexagonal $R_3Au_7Sn_3$ ($R = Y, Gd$) may be extracted from the various -COHP curves (Figure 11) and their respective integrated values (-ICOHP), which are listed in the Tables S1 and S2. Based on the band structure calculations employing the VASP code, the Gd f -states show extremely small dispersions, which typically indicate rather localized states. Therefore, the Gd f -states were treated as core-like states for all LMTO-based calculations on the gadolinium-containing structure (see Computations details). A direct comparison of the -COHP curves and the -ICOHP values for both hexagonal structures cannot be accomplished, as the average electrostatic potential is set to an arbitrary “zero” energy with varying relative positions for dissimilar systems.⁴⁷ However, close examinations of the -COHP curves and their respective integrated values for $R_3Au_7Sn_3$ ($R = Y, Gd$) revealed that both compounds exhibit alike overall bonding tendencies and, hence, the prototypical $Gd_3Au_7Sn_3$ will be selected for further bonding analysis.

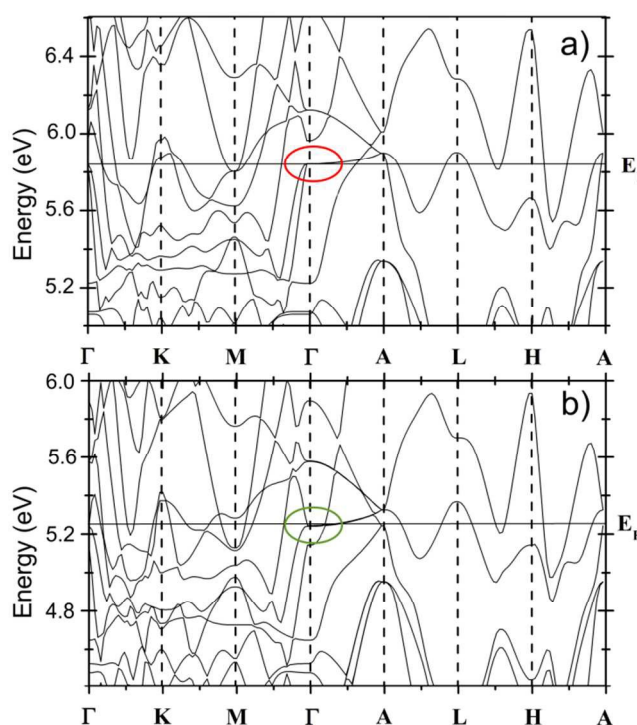


Figure 12 Band structures of (a) $Y_3Au_7Sn_3$ (top) and (b) $Gd_3Au_7Sn_3$ (bottom) around the Fermi level, E_F ; a saddle point (marked by the red circle) is evident at E_F in $Y_3Au_7Sn_3$.

Because -ICOHP values have a tendency to scale similarly to bond strength, typically the magnitude of the -ICOHP values will increase, as the bond lengths are decreased. For instance, the Au-Sn separations range from 2.753 to 2.952 Å and possess the largest -ICOHP values ranging from 1.60 to 1.22 eV/bond. An analysis of the -COHP curves reveals that extensive Au-Sn bonding interactions occur below the Fermi level, while nonbonding and antibonding Au-Sn states, are inherent in the energy regions near and above E_F , respectively. The majority of these bonding populations arise largely from the contacts between the Sn4/Sn5 sites and Au2 atoms, which surround them and construct the alternating slabs within the ab plane. Above all, significant interactions are evident for the Au1-Sn4 contacts ($d = 2.753$ Å) with the largest -ICOHP value of 1.5987 eV/bond.

The homoatomic Au–Au COHPs are optimized at -1.6 eV and remain nonbonding till E_F , which typically indicates a less bonding character relative to the heteroatomic Au–Sn, Gd–Au and Gd–Sn interactions; yet, the magnitudes of the Au–Au $-ICOHP$ values range from 0.3824 to 1.2693 eV/bond and, therefore, suggest a rather bonding character for these contacts ($d = 2.906 - 3.339$ Å). The repulsion of the Au d -states results in strongly antibonding characters of the Au–Au COHPs at around -4 eV, which is observed typically for relatively Au-rich compounds.⁴⁸ The Au2–Au2 separations within the slabs range from 3.147 to 3.339 Å and exhibit moderate $-ICOHP$ values from 0.6790 to 0.3824 eV/bond. Comparatively, the largest bonding population originates from the Au2–Au2 contacts between the slabs ($d = 2.906$ Å), while significant Au–Au interactions are also evident for the contacts between the Au2 sites and the Au1 atoms ($d = 2.960$ Å) residing in the voids of the Au@Au₆ formations. Yet, the Au2–Au2 separations, which comprise the triangular faces of the Au@Au₆ units, are 4.467 Å and show a negligible $-ICOHP$ value of -0.0219 eV/bond. Such relatively weak interactions within the triangular faces of the Au@Au₆ groups mean that the Au₇ units should be depicted as propeller-fashioned, three vertices-sharing, isosceles Au₃ triangles (Figure 2) rather than hexagonal Au₆ prisms encapsulating Au atoms. To the best of our knowledge, no structural analogue to such Au₇ composition has been reported for other polar intermetallic phases. It is worth noting that isolated Au₇ clusters have been recently reported to be stabilized by phosphine ligands,^{49,50} but, still, these agglomerates adopt mono-bridged bitetrahedral or pentagonal bipyramidal-fashioned rather than propeller-like configurations.

In addition to the Au1 atoms, gadolinium atoms are intercalated between the layers formed by the Au2 and Sn4/5 sites within the ab plane. An inspection of $-COHP$ curves and their respective $-ICOHP$ values for the Au–Gd contacts indicates bonding interactions between the Au2 and Gd3 as well as the Au1 and Gd3 atoms. More specifically, these interactions are evident below and above the Fermi level and traverse to antibonding states at 3.06 eV. In addition, the $-ICOHP$ values range from 0.5423 to 0.7788 eV/bond for the Au2–Gd3 contacts ($d = 3.025 - 3.266$ Å), while the largest $-ICOHP$ value of 0.8706 eV/bond comes from the Au1–Gd3 interactions ($d = 2.956$ Å). Note that the magnitudes of the Au–Gd interactions are smaller than those for the Au–Sn contacts, which may be regarded as a conclusive hint for a less bonding (“covalent”) character relative to the Au–Sn states. Based on Allred’s electronegativities,³⁶ in which Au (2.54) is more electronegative than Sn (1.96) and Gd (1.20), respectively, less electron withdrawal can be expected from the Gd atoms guiding to a rather polar (Au–Gd) interaction, which is well recognized for other rare-earth late transition metal compounds.^{51,52}

Experimental

Syntheses. Starting materials for the preparations of $R_3Au_7Sn_3$ ($R = Y, Gd$) were fillings of Y and Gd produced from high-purity ingots (Materials Preparation Center of the Ames Laboratory,⁵³ 99.9+ wt.%), Sn ingots (Alfa Aesar, 99.999 wt.%) and Au pieces (BASF, 99.999 wt.%). Single crystals of both compounds were obtained from reaction mixtures of 260–400 mg total, which were loaded in pre-cleaned, on-side Ar-arc welded tantalum containers inside an Ar-filled glove box ($O_2 < 0.1$ ppm, $H_2O < 0.1$ ppm). The Ta tubes were then closed inside the glove box, sealed at the other end and jacketed with evacuated Schlenk flasks. The reaction mixtures were first heated to 850 °C in 4 h, kept at that temperature for 2 h, cooled to 750 °C in 2 h, annealed at that temperature for 10 h, slowly-cooled to 300 °C with a rate of 3 °C/h and quenched in water. The products

appeared as black polyhedral chunks with metallic lustre, which are stable in air – an observation made previously for related Au-rich phases.²⁸

To get single phase samples suited for physical properties measurements, stoichiometric ratios of the elements were weighed (3–4 g total) and arc-melted under pure Ar atmosphere. The metal buttons were re-melted four times, turning them upside-down each time for better homogenization; weight losses were below 0.4 %. The alloys were wrapped in Ta foil, sealed under vacuum in quartz ampoules, annealed at 1000 °C for one week and, finally, slowly cooled to room temperature.

Table 1. Details of the crystal structure investigations and refinements for $Y_3Au_7Sn_3$ and $Gd_3Au_7Sn_3$.

Emp. Form.	$Y_3Au_7Sn_3$	$Gd_3Au_7Sn_3$
Formula Weight.	2001.57	2206.59
Space group	$P6_3/m$ (no. 176)	
a [Å]	8.148(1)	8.185(3)
c [Å]	9.394(2)	9.415(3)
Volume [Å ³]	540.1(2)	546.2(4)
Z	2	
Density [g/cm ³]	12.307	13.416
μ [mm ⁻¹]	117.273	118.165
$F(000)$	1640	1790
θ range [deg]	2.17° to 27.49°	4.98° to 26.06°
Index ranges	$-9 \leq h \leq 10$	$-10 \leq h \leq 10$
	$-10 \leq k \leq 10$	$-10 \leq k \leq 9$
Reflections collected	$-12 \leq l \leq 6$	$-11 \leq l \leq 11$
	3357	2917
Independent reflections	439	385
Refinement method	Full-matrix least-squares on F^2	
Data/restraints/parameter	439/0/25	385/0/25
Goodness-of-fit on F^2	1.05	1.10
R indices [$I > 2\sigma(I)$] ^a	$R1=0.030,$ $wR^2=0.059$	$R1=0.029,$ $wR^2=0.059$
R indices (all data)	$R1=0.045,$ $wR^2=0.065$	$R1=0.039,$ $wR^2=0.062$
R_{int}	0.061	0.078
Largest diff. peak and hole, $e^-/\text{Å}^3$	2.294 and -3.547	3.000 and -2.813
BASF parameter	0.498	0.197

X-ray diffraction studies. The purities of the products were checked from detailed phase and Rietveld analyses of sets of powder X-ray diffraction patterns, which were collected on STOE STADI P (Stoe & Cie, Darmstadt, Germany; area detector; Cu- $K_{\alpha 1}$ radiation, $\lambda = 1.54059$ Å) and Philips X’Pert (Philips, Amsterdam; point detector; Cu- $K_{\alpha 1}$ radiation, $\lambda = 1.54059$ Å) diffractometers, respectively,

at room temperature. The bulk samples were pulverized, dispersed on Mylar sheets with vacuum grease and fixed in place by split Al rings. Additional peak calibrations were accomplished against an external silicon standard for an accurate determination of the lattice parameters. The WinXPow software package⁵⁴ was utilized to edit the raw data and to analyze the obtained phases. The phase analyses of the powder X-ray diffraction patterns revealed that the samples were single phase, or high yield, products (> 97 mol.%) containing a small percentage of the binary compound AuSn (Figure S1, Supporting Information).

Single crystals were selected from the bulk, fixed on glass fibers with vacuum grease and mounted on an APEX CCD diffractometer (Bruker Inc., Madison, USA). Sets of single-crystal X-ray intensity data were collected at room temperature (~ 296 K) with Mo-K α radiation ($\lambda = 0.71073 \text{ \AA}$) in φ - and ω -scan modes with at least 750 frames and exposures of 15 s per frame. The raw reflection intensities were integrated with the aid of the SAINT program as implanted in the SMART⁵⁵ software package, while empirical absorption corrections were carried out with the program SADABS.⁵⁶

Table 2. Atomic coordinates and equivalent displacement parameters for $R_3\text{Au}_7\text{Sn}_3$ ($R = \text{Y, Gd}$).

Atom	Position	x	y	z	$U_{\text{eq}}, \text{\AA}^2$
$\text{Y}_3\text{Au}_7\text{Sn}_3$					
Au1	2d	$\frac{2}{3}$	$\frac{1}{3}$	$\frac{1}{4}$	0.0099(4)
Au2	12i	0.3481(1)	0.0182(1)	0.0955(1)	0.0112(3)
Y3	6h	0.3062(4)	0.3297(4)	$\frac{1}{4}$	0.0117(5)
Sn4	4f	$\frac{1}{3}$	$\frac{2}{3}$	0.0432(2)	0.0066(5)
Sn5	2b	0	0	0	0.0191(8)
$\text{Gd}_3\text{Au}_7\text{Sn}_3$					
Au1	2d	$\frac{2}{3}$	$\frac{1}{3}$	$\frac{1}{4}$	0.0078(4)
Au2	12i	0.3520(1)	0.0178(1)	0.0957(1)	0.0085(3)
Gd3	6h	0.2993(2)	0.3204(2)	$\frac{1}{4}$	0.0060(3)
Sn4	4f	$\frac{1}{3}$	$\frac{2}{3}$	0.0424(2)	0.0057(5)
Sn5	2b	0	0	0	0.0058(7)

The XPREP algorithms in the SHELXTL software package were employed for a proper determination of the space group $P6_3/m$ (no. 176), which was used for the final refinement of the crystal structures. The structures were solved utilizing direct methods (SHELXS-97), while full-matrix least-square refinements on F^2 with anisotropic atomic displacement parameters were accomplished with the SHELXL-97 program.⁵⁷ The initial structure solutions remained a number of relatively high residual density peaks and close inspections of the reciprocal space for the collected intensity data sets indicated twinning by merohedry. Accordingly, a twinning matrix of $\begin{pmatrix} 0 & 1 & 0 \\ 1 & 0 & 0 \\ 0 & 0 & -1 \end{pmatrix}$ has been applied to correct the intensity data and to include all measured reflections in the structure refinements. The following refinements did not indicate any significant peaks and resulted in BASF values of 0.197 and 0.498 for the Gd- and Y-containing compounds, respectively. With these settings the R_1 -factor converged to 0.0295 and 0.030 (Table 1). Analyses for a possible higher symmetry with the aid of the ADDSYM algorithm in the PLATON software package⁵⁸ resulted in the space group $P6_3/mcm$. However, further refinements did not lead to any reasonable structure solution and provided an extra proof for the presence of twinning by merohedry. Further details of the single crystal structure investigations may be obtained from the Fachinformationszentrum Karlsruhe, 76344 Eggenstein-Leopoldshafen, Germany (Fax: +49-

7247-808-666; E-Mail: crysdata@fiz-karlsruhe.de; <http://www.fiz-karlsruhe.de/request> for deposited data.html) on quoting the depository numbers 429573 and 429572 for $\text{Gd}_3\text{Au}_7\text{Sn}_3$ and $\text{Y}_3\text{Au}_7\text{Sn}_3$, respectively.

Physical properties measurements. Heat capacity data were collected from 1.8 to 300 K using the semi-adiabatic, heat pulse method; a Lake Shore germanium resistance thermometer (GRT) was used as the temperature sensor. The DC magnetization was measured as a function of both temperature (in the range 2-300 K) and applied magnetic fields (0 to 5 T) using a Magnetic Property Measurement System (MPMS, Quantum Design, San Diego, USA). Resistivity measurements were carried out between 1.8 and 300 K by the four-probe dc method using a current of 50 mA, while a Lake Shore silicon diode was used to measure the temperature.

Computational details. To provide an insight into the electronic and magnetic structure for $\text{Gd}_3\text{Au}_7\text{Sn}_3$, three different spin ordering models within the Gd lattices were examined as starting points for the density functional theory (DFT) based calculations. Furthermore, the electronic structure of the yttrium-containing compound was analyzed to account for the physical properties of this structure. The DFT computations in the generalized-gradient approximation (GGA) of Perdew, Burke and Enzerhof⁵⁹ (PBE) were carried out utilizing the projector-augmented wave (PAW) method of Blöchl⁶⁰ as adapted in the Vienna ab initio Simulation Package (VASP) code by Kresse and Joubert.⁶¹⁻⁶⁵ A Hubbard U correctional parameter ($U = 6 \text{ eV}$) was applied to account for the strong correlations within the localized Gd-4f states. The energy cutoffs of the plane wave basis sets were set to 500 eV, while starting meshes of $4 \times 4 \times 4$ up to $8 \times 8 \times 8$ k -points were used to sample the first Brillouin zones for reciprocal space integrations. Structural optimizations were included for all calculations until energy difference between two iterations fell below 0.01 meV/cell.

A chemical bonding analysis on the electronic structures of $\text{Y}_3\text{Au}_7\text{Sn}_3$ and $\text{Gd}_3\text{Au}_7\text{Sn}_3$ was accomplished based on the crystal orbital Hamilton populations (COHP) and their respective integrated values (ICOHP), which were computed using the tight-binding linear-muffin-tin orbital (TB-LMTO) method with the atomic sphere approximation (ASA) in the Stuttgart code.^{66,67} In particular, the off-site projected DOS are weighted with the respective Hamilton matrix elements, which allow the identification of antibonding and bonding contributions within the structure.⁶⁸ The Wigner-Seitz (WS) radii were generated automatically and empty spheres (ES) were assigned to guarantee an optimal approximation of full potentials. The following orbitals were utilized in the basis set (downfolded⁶⁹ orbitals in parentheses): Au-6s/(-6p)/-5d/(-5f); Y-5s/(-5p)/-4d/(-4f); Gd-6s/(-6p)/-5d; Sn-5s/(-5p)/(-5d)/(-4f). The corresponding WS radii were [\AA]: Au: 2.90-3.04; Y: 3.48; Gd: 3.53; Sn: 3.09-3.39. The DOS obtained from the VASP computations revealed that the Gd-4f states are strongly localized and, accordingly, these states were treated as core-like states in accord with previous calculations on R-containing intermetallic compounds.⁷⁰ Reciprocal space integrations were performed with the tetrahedron method⁷¹ using 224 irreducible k -points.

Conclusions

Two novel polar intermetallic compounds $\text{Y}_3\text{Au}_7\text{Sn}_3$ (**I**) and $\text{Gd}_3\text{Au}_7\text{Sn}_3$ (**II**) have been synthesized and their crystal structures have been determined by single crystal X-ray diffraction. They crystallize with a hexagonal unit cell ($P6_3/m$, $Z = 2$) and consist of paral-

lel slabs of Sn centred edge-sharing Au₆ trigonal antiprisms, which intercalate R₃ triangles and additional Au atoms. The latter reside in the centres of unique Au@Au₆ formations, which can be depicted as propeller-fashioned, three vertices-sharing, isosceles (almost equilateral) Au₃ triangles.

The magnetic susceptibility data for the gadolinium-containing compound exhibits an antiferromagnetic ordering below 13 K, while a Pauli paramagnetic behaviour is observed for the yttrium-containing analogue. The electrical resistivity shows metallic behaviour for both compounds, with a clear anomaly in **II** in correspondence of the magnetic transition, and a downward curvature for **I** at about 1.9 K suggesting a superconducting transition in this compound. The band structure calculations of both compounds are in full accordance with the physical properties, as the positions of the Fermi levels in both structures suggest metallic conductivities.

The bonding is dominated by heteroatomic Au–Sn and Au–Gd contacts within and between the Au₆Sn slabs, respectively, while homoatomic Au–Au contacts play a subordinate role in the overall picture. Yet, homoatomic Au–Au bonding is evident within the Au@Au₆ units, which are incorporated between the Au₆Sn slabs. An examination of the states near the Fermi level suggests that the structure attempts to optimize overall bonding through the full occupation of the heteroatomic Au–Sn bonding states, which cross to antibonding states at –0.09 eV.

Acknowledgements

This work was supported by the Office of the Basic Energy Sciences, Materials Sciences Division, U. S. Department of Energy (DOE) and by the Critical Materials Institute, an Energy Innovation Hub funded by the U.S. Department of Energy, Office of Energy Efficiency and Renewable Energy, Advanced Manufacturing Office as well as the Department of Materials Science and Engineering at Iowa State University. Ames Laboratory is operated for DOE by Iowa State University under contract No. DE-AC02-07CH11358. The authors would like to thank Prof. Maria Luisa Fornasini and Prof. Karl A. Gschneidner Jr. for their helpful comments.

Notes and references

^aThe Ames Laboratory, U.S. Department of Energy, Iowa State University, Ames, IA 50011, USA

^bDepartment of Chemistry, University of Genova, Via Dodecaneso 31, 16146 Genova, Italy

^cDepartment of Materials Science and Engineering, Iowa State University, Ames, IA 50011, USA

^dDepartment of Matter Physics & Materials Science, Tata Institute of Fundamental Research, T.I.F.R. Homi Bhabha Road, Mumbai 400 005, India

^eInstitute SPIN-CNR, Corso Perrone 24, 16152 Genova, Italy.

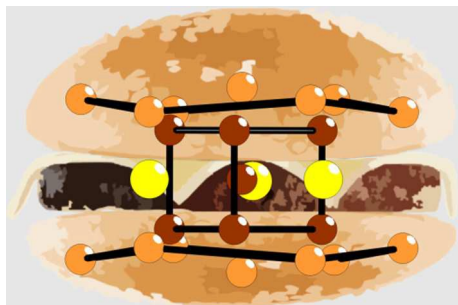
*E-mail: mudring@iastate.edu, chimfis@chimica.unige.it

† Electronic Supplementary Information (ESI) available: measured and simulated powder X-Ray diffraction patterns of R₃Au₇Sn₃ (R = Y, Gd), representations of the site and orbital projected DOS curves as well as the different AFM spin ordering models of Gd₃Au₇Sn₃ and tables with distances, multiplicities and –ICOHP values for selected contacts in both Y₃Au₇Sn₃ and Gd₃Au₇Sn₃. See DOI: 10.1039/b000000x/

- (1) Corbett, J. D. *Inorg. Chem.* **2010**, *49*, 13–28.
- (2) Rossi, D.; Marazza, R.; Ferro, R. *J. Alloys Compd.* **1992**, *187*, 267–270.
- (3) Rossi, D.; Ferro, R. *J. Alloys Compd.* **2001**, *317–318*, 521–524.
- (4) Pöttgen, R. *Z. Naturforsch.* **2006**, *61b*, 677–698.
- (5) Pöttgen, R. *Z. Naturforsch.* **1994**, *49b*, 1309–1313.
- (6) Pöttgen, R. *Z. Naturforsch.* **1994**, *49b*, 1525–1530.
- (7) Kraft, R.; Pöttgen, R.; Kaczorowski, D. *Chem. Mater.* **2003**, *15*, 2998–3002.

- (8) Goldman, A.; Kong, T.; Kreyssig, A.; Jesche, A.; Ramazanoglu, M.; Dennis, K.; Bud'ko, S.; Canfield, P. C. *Nat. Mater.* **2013**, *12*, 714–718.
- (9) Steurer, W.; Deloudi, S. *Crystallography of Quasicrystals*, Springer, Berlin, **2009**.
- (10) Pyykkö, P. *Chem. Rev.* **1988**, *88*, 563.
- (11) Pyykkö, P. *Angew. Chem. Int. Ed.* **2004**, *43*, 4412–4456.
- (12) Li, B.; Kim, S.-J.; Miller, G. J.; Corbett, J. D. *Inorg. Chem.* **2009**, *48*, 6573–6583.
- (13) Smetana, V.; Corbett, J. D.; Miller, G. J. *J. Solid State Chem.* **2013**, *207*, 21–28.
- (14) Smetana, V.; Miller, G. J.; Corbett, J. D. *Inorg. Chem.* **2013**, *52*, 12502–12510.
- (15) Lin, Q.; Corbett, J. D. *Inorg. Chem.* **2011**, *50*, 1808–1815.
- (16) Lin, Q.; Corbett, J. D. *Inorg. Chem.* **2007**, *46*, 8722–8727.
- (17) Lin, Q.; Smetana, V.; Miller, G. J.; Corbett, J. D. *Inorg. Chem.* **2012**, *51*, 8882–8889.
- (18) Smetana, V.; Miller, G. J.; Corbett, J. D. *Inorg. Chem.* **2012**, *51*, 7711–7721.
- (19) Smetana, V.; Corbett, J. D.; Miller, G. J. *Inorg. Chem.* **2012**, *51*, 1695–1702.
- (20) Smetana, V.; Lin, Q.; Pratt, D.; Kreyssig, A.; Ramazanoglu, M.; Corbett, J. D.; Goldman, A.; Miller, G. J. *Angew. Chem. Int. Ed.* **2012**, *51*, 12699–12702.
- (21) Lin, Q.; Corbett, J. D. *Inorg. Chem.* **2008**, *47*, 7651–7659.
- (22) Fornasini, M. L.; Manfrinetti, P.; Mazzone, D. *Z. Krist. NCS* **2010**, *225*, 221–222.
- (23) Fornasini, M. L.; Mazzone, D.; Provino, A.; Michetti, M.; Paudyal, D.; Gschneidner, K. A. J.; Manfrinetti, P. *Intermetallics* **2014**, *53*, 169–176.
- (24) de Mooij, D.; Buschow, K. J. *Less-Common Met.* **1984**, *102*, 113–117.
- (25) Wenski, G.; Mewis, A. Z. *Anorg. Allg. Chem.* **1986**, *535*, 110–122.
- (26) Cotton, S. *Lanthanide and Actinide Chemistry*; John Wiley & Sons Ltd.: Chichester, 2006.
- (27) Cordero, B.; Gomez, V.; Platero-Prats, A.; Reves, M.; Echeverria, J.; Cremades, E.; Barragan, F.; Alvarez, S. *Dalton Trans.* **2008**, *2008*, 2832–2838.
- (28) Lin, Q.; Mishra, T.; Corbett, J. D. *J. Am. Chem. Soc.* **2013**, *135*, 11023–11031.
- (29) Mishra, T.; Lin, Q.; Corbett, J. D. *Inorg. Chem.* **2013**, *52*, 13623–13630.
- (30) Palasyuk, A.; Grin, Y.; Miller, G. J. *J. Am. Chem. Soc.* **2014**, *136*, 3108–3117.
- (31) Gerke, B.; Hoffmann, R. D.; Pöttgen, R. *Z. Anorg. Allg. Chem.* **2013**, *639*, 2444–2449.
- (32) Smetana, V.; Steinberg, S.; Card, N.; Mudring, A.-V.; Miller, G. J. *Inorg. Chem.* **2015**, *54*, 1010–1018.
- (33) Gerke, B.; Pöttgen, R. *Z. Naturforsch.* **2014**, *69b*, 121–124.
- (34) Sinnen, H. D.; Schuster, H. U. *Z. Naturforsch. B* **1981**, *36*, 833–836.
- (35) Lenz, J.; Schubert, K. *Monatsh. Chem.* **1971**, *102*, 1689–1698.
- (36) Allred, A. L. *J. Inorg. Nucl. Chem.* **1961**, *17*, 215–221.
- (37) Dwight, A. *Proc. Rare Earth Res. Conf.* **1976**, *1*, 480–489.
- (38) Nielsen, J. W.; Baenziger, N. C. *Acta Crystallogr.* **1954**, *7*, 132–133.
- (39) Lee, C. H.; Whangbo, M.; Köhler, J. *Z. Anorg. Allg. Chem.* **2007**, *633*, 2631–2634.
- (40) Bockelmann, W.; Jacobs, H.; Schuster, H. U. *Z. Naturforsch.* **1970**, *25b*, 1305–1306.
- (41) Ramirez, A. P. *Annu. Rev. Mater. Sci.* **1994**, *24*, 453–480.
- (42) Bouvier, M.; Lethuillier, P.; Schmitt, D. *Phys. Rev. B* **1991**, *43*, 13137.
- (43) Tao, K.; Zhou, J.; Sun, Q.; Wang, Q.; Stepanyuk, V. S.; Jena, P. *Phys. Rev. B* **2014**, *89*, 085103.
- (44) Birch, F. *Phys. Rev.* **1947**, *71*, 809–824.
- (45) van Hove, L. *Phys. Rev.* **1953**, *89*, 1189–1193.
- (46) Simon, A. *Angew. Chem. Int. Ed. Engl.* **1997**, *36*, 1788–1806.
- (47) Dronskowski, R. *Computational Chemistry of Solid State Materials*; Wiley-VCH: Weinheim, **2005**.
- (48) Köhler, J.; Whangbo, M.-H. *Solid State Sci.* **2008**, *10*, 444–449.
- (49) Schulz-Dobrick, M.; Jansen, M. *Angew. Chem. Int. Ed.* **2008**, *47*, 2256–2259.

- (50) Shichibu, Y.; Zhang, M.; Kamei, Y.; Konishi, K. *J. Am. Chem. Soc.* **2014**, *136*, 12892–12895.
- (51) Samal, S. L.; Pandey, A.; Johnston, D. C.; Corbett, J. D. *J. Am. Chem. Soc.* **2013**, *135*, 910–917.
- (52) Samal, S. L.; Pandey, A.; Johnston, D. C.; Corbett, J. D.; Miller, G. J. *Chem. Mater.* **2014**, *26*, 3209–3218.
- (53) *Materials Preparation Center, The Ames Laboratory, US Department of Energy, Ames, IA, USA, www.mpc.ameslab.gov.*
- (54) Stoe & Cie GmbH: Darmstadt, Germany, 2004.
- (55) Bruker AXS, Inc.: Madison, WI, 1996.
- (56) Blessing, R. *Acta Crystallogr., Sect. A* **1995**, *51*, 33–38.
- (57) Sheldrick, G. M. *Acta Crystallogr., Sect. A* **2008**, *64*, 112–122.
- (58) Spek, A. L. *Acta Crystallogr., Sect. D* **2009**, *65*, 148–155.
- (59) Perdew, J. P.; Burke, K.; Ernzenhof, M. *Phys. Rev. Lett.* **1996**, *77*, 3865–3868.
- (60) Blöchl, P. E. *Phys. Rev. B* **1994**, *50*, 17953–17979.
- (61) Kresse, G.; Marsman, M.; Furthmüller, J. *Vienna Ab initio Simulation Package (VASP) VASP, the user Guide* **2010**.
- (62) Kresse, G.; Furthmüller, J. *J. Comput. Mat. Sci.* **1996**, *6*, 15–50.
- (63) Kresse, G.; Furthmüller, J. *Phys. Rev. B* **1996**, *54*, 11169–11186.
- (64) Kresse, G.; Hafner, J. *Phys. Rev. B* **1993**, *47*, 558–561.
- (65) Kresse, G.; Joubert, D. *Phys. Rev. B* **1999**, *59*, 1758–1775.
- (66) Tank, R.; Jepsen, O.; Burkhardt, A.; Andersen, O. K.; Max-Planck-Institut für Festkörperforschung: Stuttgart, Germany, 1994.
- (67) Andersen, O. K.; Jepsen, O. *Phys. Rev. Lett.* **1984**, *53*, 2571–2574.
- (68) Dronskowski, R.; Blöchl, P. E. *J. Phys. Chem.* **1993**, *97*, 8617–8624.
- (69) Lambrecht, W. R. L.; Andersen, O. K. *Phys. Rev. B* **1986**, *34*, 2439–2449.
- (70) Chai, P.; Corbett, J. D. *Inorg. Chem.* **2012**, *51*, 3548–3556.
- (71) Blöchl, P. E.; Jepsen, O.; Andersen, O. K. *Phys. Rev. B* **1994**, *49*, 16223–16233.



For table of contents only. Gd₃ capped Au@Au₆ cluster sandwiched between two hexagonal Sn layers.